



Performance evaluation of RC-MRFs with UHPSFRC and SMA rebars subjected to mainshock-aftershock sequences

Marziyeh Ghasemi^a, Hossein Khorshidi^b, Nader Fanaie^{b,*}

^a Department of Civil Engineering, Babol Noshirvani University of Technology, Mazandaran, Iran

^b Department of Civil Engineering, K. N. Toosi University of Technology, Tehran, Iran

ARTICLE INFO

Keywords:

Mainshock-aftershock
Seismic sequence
Reinforced Concrete (RC) frame
Shape Memory Alloy (SMA)
Ultra-High- Performance Steel Fiber Reinforced Concrete (UHPSFRC)

ABSTRACT

Although structures are generally subjected to mainshock-aftershock sequences, the current structural design process merely considers the main seismic event. This study aims to compare the performance of Reinforced Concrete Moment Resisting Frames (RC-MRFs) with Shape Memory Alloy (SMA) and Ultra-High-Performance Steel Fiber Reinforced Concrete (UHPSFRC) under the influences of mainshock and aftershock sequence. To achieve this aim, 3, 6, and 8-story five-span frames were simulated considering three different approaches: (i) RC frames; (ii) RC frames with SMA rebars in the plastic hinge length of the beams; (iii) RC frames with UHPSFRC and SMA in the plastic hinge length of the beams.

Each frame was analyzed under two different scenarios, with and without considering seismic sequences to assess the post-earthquake performance of damaged RC frames. Time history analyses were conducted using seven real accelerograms. Maximum transient inter-story and roof drifts, as well as residual inter-story drifts, were determined and compared in undamaged and damaged structures to assess the effect of seismic sequence. As the performance evaluation of the damaged structures appears to be essential to make repair policy decisions and rescue operations, damage states were defined according to FEMA-356 based on maximum transient and residual drifts. Numerical results illustrate the salient effect of using SMA and UHPSFRC synergistically in reducing transient and residual drifts and enhancing the functionality of structures in both mainshock and aftershock.

1. Introduction

Current structural design codes, which are based on conventional seismic design strategies, consider one earthquake as the mainshock event, while the post-earthquake scenarios and its effects are generally neglected. Structures are frequently not merely subjected to a single earthquake event called the mainshock, but also to a mainshock-aftershock sequence. Aftershocks occur during the following days to years with different magnitude, duration, frequency, amplitude, and other characteristics compared to the corresponded mainshock. For instance, an earthquake with a magnitude (M_w) 7.8 struck Gorkha, Nepal on 25 April 2015, which caused fatalities as well as widespread structural damages, was followed by a series of aftershocks, including an M_w 7.3 event on May 12, 2015 [1].

Since aftershocks might occur in a short time after the mainshock, repair or retrofit activities are often impractical, and identifying the damaged structures after a major earthquake is critical. Several studies

have investigated the effects and properties of the aftershocks in a seismic sequence, such as the 1994 Northridge earthquake, 1999 Kocaeli earthquake, and 2015 Gorkha earthquake [2–4].

Over the past years, numerous studies have been carried out to assess the performance of concrete and steel buildings during seismic sequences. Guo et al. [5] investigated the incremental seismic damage development in RC frames subjected to seismic sequences. Raghunandan et al. [6] studied the aftershock collapse vulnerability of ductile reinforced concrete frames. They showed that considerable damages due to the mainshock decrease the average collapse capacity of the frame by 40% to resist aftershock. However, the aftershock collapse fragility of the building which is not severely damaged during the mainshock is not changed significantly. Jeon et al. [7] studied the aftershock fragility curves of RC frames damaged by the mainshock. The results of their study proved that damage vulnerability increases for frames with considerable damage caused by the mainshock. Furtado et al. [8] assessed the mainshock-aftershock damage of in-filled RC frames. An 8-

* Corresponding author.

E-mail addresses: marziyeh.ghasemi.r@gmail.com (M. Ghasemi), hossein.khorshidi@mail.kntu.ac.ir (H. Khorshidi), fanaie@kntu.ac.ir (N. Fanaie).

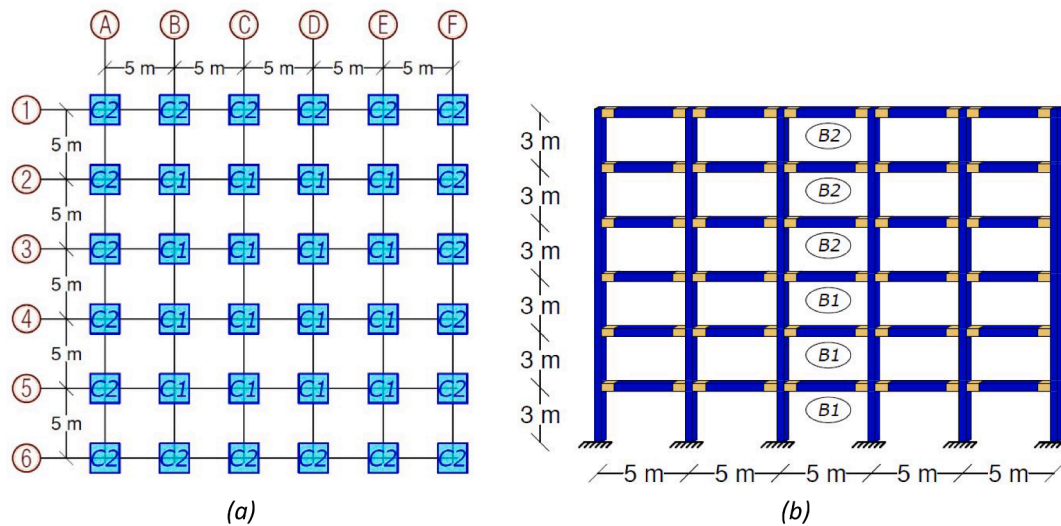


Fig. 1. (a) Plan view, (b) Elevation view.

story RC structure with infill walls with and without considering out-of-plane non-linear behavior was investigated. In this study, a methodology to perform seismic assessment of damaged structures due to seismic sequences was proposed. They also assessed the seismic vulnerability of undamaged and damaged intended structures. Shafaei and Naderpour [9] conducted a study on the behavior of ordinary RC frames retrofitted with Fiber Reinforced Polymers (FRPs) exposed to seismic sequences. Their study confirmed that whilst FRP enhances the collapse capacity, the aftershock plays an important role in reducing the structural capacity of retrofitted frames. Dong and Frangopol [10] presented a framework for probabilistic seismic performance evaluation of highway bridges exposed to mainshock-aftershock.

Recently, various methods have been employed to improve the performance of RC structures, including using different steel braces to retrofit RC frames [11], Glass Fiber Reinforced Polymer (GFRP) bars [12], super-elastic shape memory alloy rebars [13–16], SMA-FRP reinforced concrete [17], SMA bars and ultra-high performance concrete in the critical zones of the structures [18], high-performance concrete and very-high-performance concrete elements with Ni-Ti reinforcements [19], and the Engineered Cementitious Composites (ECC) in the beam-column joints [20,21].

SMA has gained acceptance as one of the construction materials in civil engineering applications due to their characteristics, such as the capability to tolerate cyclic deformations and energy dissipation [22]. SMAs have two fundamental properties: Super-elasticity Effect (SE) and Shape Memory Effect (SME). While SMAs with SE can recover their initial shape after loading and unloading, SMAs with SME return to their first shape by heating [23]. A variety of compositions have been used in SMA, while Ni-Ti which refers to Nickel and Titanium is the most suitable composition for structural achievement due to its large recoverable strain, super-elasticity, and corrosion resistance [24]. In this paper, SMA refers to those made up of Ni-Ti.

UHPSFRC is a novel material that has been recently introduced to protect civil engineering structures against earthquakes. Relevant studies have shown that it has multiple cracking behaviors [25] as well as high compressive strength and improved tensile strength [26].

This paper aims to investigate the maximum transient and residual drifts response of reinforced concrete moment resisting frames in which ordinary steel rebars were replaced with SMA in the plastic hinge of the beams to limit the residual drifts of the structure in seismic sequences. As SMA rebars have an elasticity modulus that is less than that of steel, greater transient drifts in the frames were expected. To deal with this problem, using UHPSFRC was suggested and conventional concrete is also replaced with UHPSFRC in the plastic hinge of the beams.

Table 1

Column size and reinforcement details.

Story ID	Floor level	Column ID			
		C1		C2	
		Size (mm)	Reinforcement	Size (mm)	Reinforcement
3-Story	1 to 3	375 × 375	8 ϕ15	300 × 300	4 ϕ 20
6-Story	1 to 3	450 × 450	8 ϕ 25	300 × 300	6 ϕ 20
	4 to 6	450 × 450	8 ϕ 20	300 × 300	4 ϕ 20
8-Story	1 to 3	500 × 500	8 ϕ 25	300 × 300	6 ϕ 25
	4 to 8	500 × 500	6 ϕ 25	300 × 300	6 ϕ 20

Mainshock-aftershock nonlinear time history analyses were conducted to study the effects of pre-existing damage in three different cases.

2. Numerical modeling of RC-MRFs

2.1. The geometry of frames

In this study, reinforced concrete buildings with different number of stories (3, 6, and 8) were extracted from the research conducted by Alam et al. [15]. The frames had a span length of 5 m along each direction and a story height of 3 m for all stories. The typical plan view and side view of the 6-story frame are illustrated in Fig. 1(a) and (b), respectively.

Tables 1 and 2 declare the size of columns and beams and reinforcement details. Fig. 2 exhibits the reinforcement details of a typical beam.

Each building had different types of material in the plastic hinge zone of the beams as denoted in Table 3. A two-part notation system was used for identification: the first letter shows the concrete type, whereas the second letter denotes the rebar type. Because the first letter of steel and SMA resulted in the same name for the models, the second letter of SMA, M, has been used for CM. Notably, the columns of all frames were made up of conventional RC.

As noted in recent studies [13,15], there is no specific difference between models that were fully reinforced with SMA in their beams and those that had SMA rebars in plastic hinge zones and steel bars in the remaining area of the beams. Thus, in order to restrict the cost of material due to using SMA, in this study the use of SMA in all parts of the beams was neglected.

In recent studies, no specific research has been conducted for computing the length of the plastic hinge in the frame elements, which are made up of UHPSFRC and SMA bars. Therefore, the Paulay and

Table 2
Beam size and main reinforcement details.

Story ID	Beam ID	Floor level	Size (mm)	Reinforcement					
				Section 1-1		Section 2-2		Section 3-3	
				Top	Bottom	Top	Bottom	Top	Bottom
3-Story	B1	1 to 3	300 × 450	2 φ 20	2 φ 20	2 φ 20	2 φ 20	2 φ 20	2 φ 20
6-Story	B1	1 to 3	300 × 500	3 φ 25	4 φ 25	3 φ 25	4 φ 25	5 φ 25	4 φ 20
	B2	4 to 6	300 × 500	2 φ 20	2 φ 20	2 φ 20	3 φ 20	2 φ 20	3 φ 20
8-Story	B1	1 to 3	300 × 500	3 φ 25	4 φ 25	3 φ 25	4 φ 25	5 φ 25	4 φ 20
	B2	4 to 6	300 × 500	3 φ 20	3 φ 20	3 φ 20	3 φ 20	3 φ 20	3 φ 20

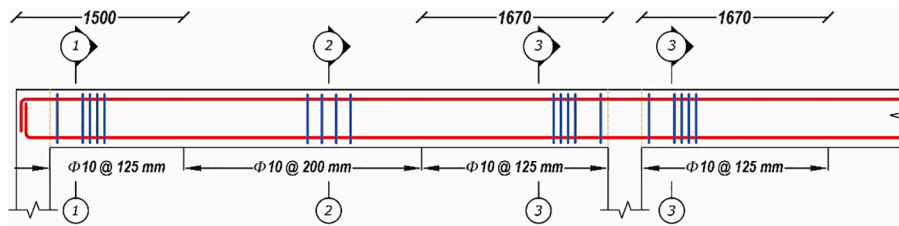


Fig. 2. Longitudinal section of beam reinforcement.

Table 3
Frames ID and relative arrangement.

Frame ID	Materials in plastic hinge length of the beams	
	Concrete	Rebar
CS	Conventional	Steel
CM	Conventional	SMA
UM	UHPSFRC	SMA

Priestley equation [27] which is also proposed by Alam et al. [28] for SMA RC frames was adopted to determine the plastic hinge length and this length was considered constant for all models. Eq. (1) presents the Paulay and Priestley equation.

$$l_p = 0.08l + 0.022d_{bl}f_{ye} \quad (1)$$

Where l_p is plastic hinge length, l is the length of the beam, d_{bl} is the diameter of the longitudinal bar and f_{ye} is longitudinal steel yield stress. The plastic hinge zone of the beams and its location is demonstrated in Fig. 1.

2.2. The finite element model of frames

To conduct this study, the OpenSees software [29] was used to perform the inelastic analyses. This software considers both geometric and material nonlinearities and is able to model the spread inelasticity along the element length and across the section by the use of fiber techniques.

Although 3D models are more authentic for the probabilistic analysis of seismic demand, in this paper, the analyses were performed on interior 2D frames selected from each of the three-dimensional structures. The reason for this simplification was to decrease the time of analysis regarding a large number of time-consuming analyses for 3D models. To assume the damping parameter in dynamic analysis, a 2.5% Rayleigh damping ratio was considered for the first and third modes.

The uniaxialMaterial Concrete 02 model was used to simulate concrete behavior with tensile strength and linear tension softening. For confined concrete material parameters, the equations proposed by Mander et al. [30] were used as represented in Eqs. (2) and (3).

$$f_c = Kf'_c \left[\frac{2\varepsilon_c}{0.002K} - \left(\frac{\varepsilon_c}{0.002K} \right)^2 \right] \quad (2)$$

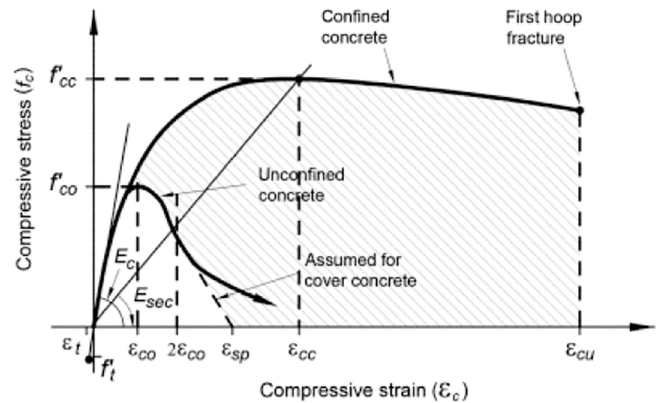


Fig. 3. Confined and unconfined concrete stress–strain curves [30].

$$K = 1 + \frac{\rho_s f_{yh}}{f'_c} \quad (3)$$

where f_{yh} is the hoops yield strength, ρ_s is the ratio of the volume of hoop reinforcement to the volume of the concrete core, f'_c and ε_c are the concrete longitudinal compressive stress and strain. In Fig. 3, variable Kf'_c and ε_{cu} are the ultimate compressive strength and compressive strain of the confined concrete.

The uniaxialMaterial Steel02 model was selected to predict the uniaxial steel material with isotropic hardening proposed by Menegotto and Pinto [31].

To simulate UHPSFRC material, the uniaxialMaterial ECC01 model was applied based on the model by Han et al. [32]. While this model is relatively simple, it is capable of reasonably describing the complex cyclic behavior of the intended material. The parameters of this model are limited and also easy to determine with simple experimental researches. In this study, the parameters for UHPSFRC material were extracted from the study conducted by He et al. [26], which were validated by experimental research undertaken by Xu et al. [33].

The uniaxialMaterial SMA was also used to capture the behavior of NiTi SMA bars in the numerical model. The behavior of SMAs is symmetric and is identical in tension and compression. This model is proposed by Fugazza [34] and is a modified version of the model by Auricchio and Sacco [35]. The advantages of this model are simplicity, a limited number of required parameters, and showing the partial and

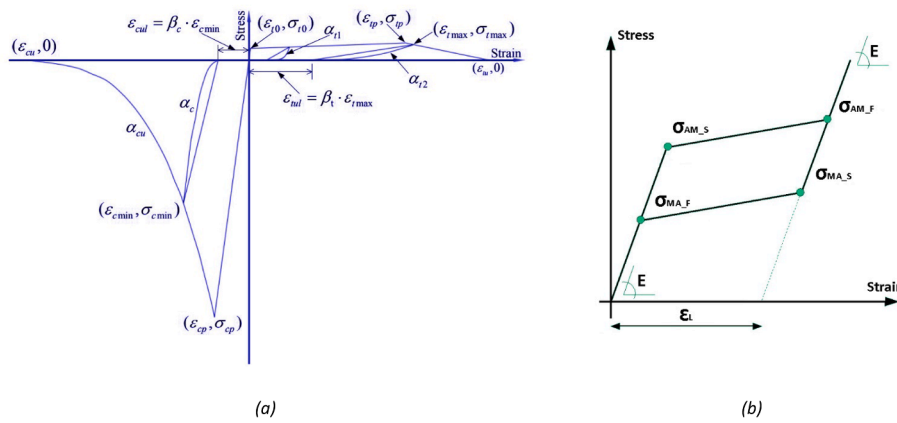


Fig. 4. Stress–strain curve of: (a) UHPSFRC, (b) SMA.

Table 4 Assumed properties of materials.

Material	Property	Value
Concrete	Compressive Strength	–35 MPa
	Tensile strength	3.5 MPa
	Strain at peak stress	0.002
Steel	Modulus of elasticity	200,000 MPa
	Yield strength	400 MPa
	Strain hardening parameter	0.005
UHPSFRC	Cracking strain (ϵ_{t0})	0.0007
	Cracking stress (σ_{t0})	8.1 MPa
	Peak strain ($\epsilon_{tp}/\epsilon_{cp}$)	0.04/–0.01
	Peak stress (σ_{tp}/σ_{cp})	14/–115 MPa
	Ultimate strain ($\epsilon_{tu}/\epsilon_{cu}$)	0.07/–0.04
	Residual strain parameter (β_t/β_c)	0.4/0.3
SMA	Modulus of elasticity (E)	60,000 MPa
	Austenite to Martensite starting stress ($\sigma_{AM,S}$)	400 MPa
	Austenite to Martensite finishing stress ($\sigma_{AM,F}$)	500 MPa
	Martensite to Austenite starting stress ($\sigma_{MA,S}$)	300 MPa
	Martensite to Austenite finishing stress ($\sigma_{MA,F}$)	100
	Super-elastic plateau strain length (ϵ_L)	6

complete phase transformations. The main disadvantage is the lack of consideration for the speed of loading and temperature in the model. This model describes the behavior of super-elastic materials under seismic loadings in terms of several hysteresis loops within the main loop (complete phase transformation). The consideration of identical elastic modulus for austenite and martensite phases is another assumption used in this model.

The stress–strain curve of UHPSFRC and SMA used in this study are indicated in Fig. 4. Table 4 reveals the assumed properties of materials

employed in the finite element model.

The fiber section was utilized to model the frame cross sections by assigning defined geometry and material, in which, for more accuracy, the core concrete was divided into 20 (in width) by 20 (in length), and cover concrete was divided into 6 (in thickness) by 20 (in length) fiber segments. The final response of the section was determined by the integration of the stress–strain response of all parts. This section provides the distributed plasticity capability for the elements.

Nonlinear displacement-based beam-column elements with distributed plasticity were applied to model the beams and columns. Fig. 5 discloses the analytical modeling technique for beams. As shown, each beam contains three various reinforcement details. In addition, in the plastic hinge of the beams (l_p), UHPSFRC and SMA rebars have been used. As illustrated in Fig. 5, seven integration points were considered in beams and columns simulation.

2.3. Validation of the numerical model

To verify the modeling approach, the TS-SS50-Lam5.3-N₀.20 column of UHPSFRC is extracted from the experimental study by Xu et al. [33]. The parameters of uniaxialMaterial ECC01 to define UHPSFRC material in numerical model are presented in Table 4, the loading protocol and other details can be found in Ref. [33]. Moreover, Youssef et al. [36] conducted an experimental study on beam-column joints reinforced with SE SMAs under reversed cyclic loading. The JBC-2 specimen in which the steel rebars in the plastic hinge region of the beam were replaced with SMA bars was employed for validation.

The adopted finite element model for UHPSFRC column and SMA beam-column joint are depicted in Fig. 6(a) and (b) respectively. The bond-slip effect in the numerical models is adopted using bond-slip

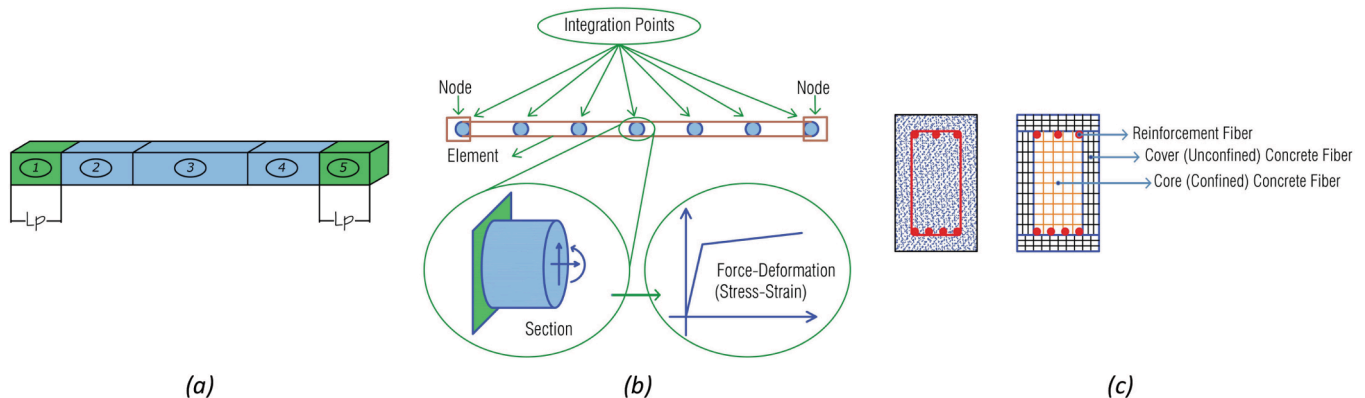


Fig. 5. The analytical technique used for simulating elements: (a) Schematic division of beam elements (b) Integration points, (c) Fiber section.

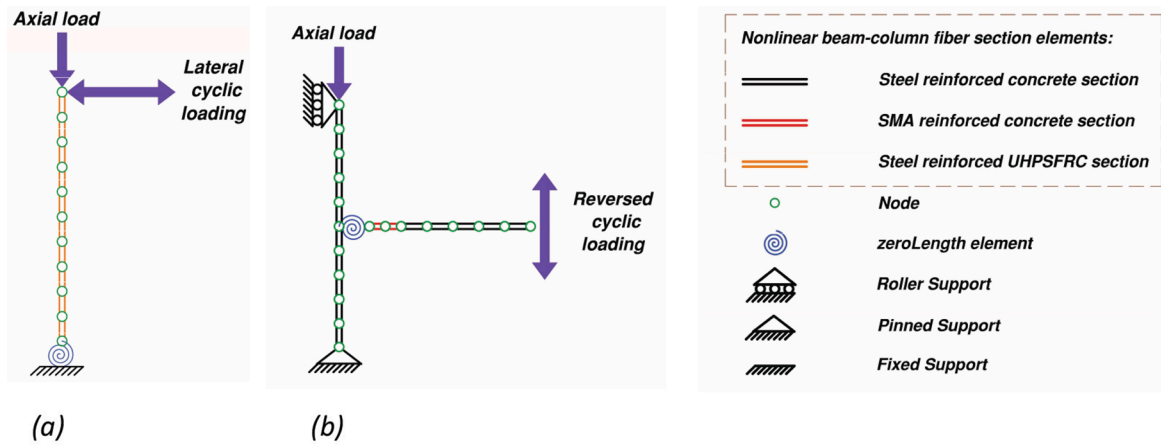


Fig. 6. The finite element models: (a) UHPSFRC column, (b) SMA beam-column joint.

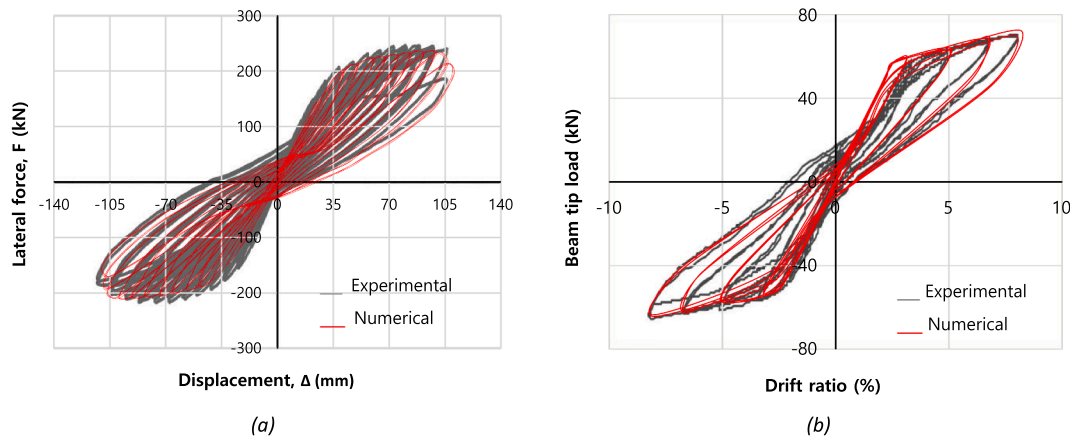


Fig. 7. The comparison between experiment and numerical results: (a) UHPSFRC column, (b) SMA beam-column joint.

spring in the zero-length element based on the study by Zhao and Sri-tharan [37], as shown in Fig. 6. As shown in Fig. 7(a), it is evident that the uniaxialMaterial ECC01 is able to simulate the hysteric behavior of UHPSFRC accurately. Fig. 7(b) shows a good agreement with the experimental results of SMA beam-column joints.

It is noted that this work is a preliminary study to investigate the use of novel materials (SMA and UHPSFRC) in RC frames. Considering the variety of materials in the beam end region of frames, and to avoid introducing many variations, in this study, it is assumed that a perfect bond exists between steel and SMA bars, and regular concrete and UHPSFRC. However, the modeling accuracy can be improved by using the zero-length element and rotational spring (as mentioned in the validation part).

2.4. Eigenvalue analysis

Table 5 presents the first mode period of the frames in this study. Eigenvalue analyses were performed to establish the fundamental period of structures and verify the accuracy of modeling and assumptions. As expected, the fundamental period of CM and UM frames increases compare to CS because of SMA’s and UHPSFRC’s lower stiffness than that of steel and concrete respectively. The periods are in agreement with the prior study which also shows the proper mass distribution from 3D to 2D model. Additionally, pushover analysis has been

Table 5
The fundamental period of frames.

Story ID	Frame ID	Fundamental period (sec)		
		This study		Ref. No. 15
		Before gravity load	After gravity load	
3-story	CS	0.40	0.45	0.39
	CM	0.41	0.46	0.41
	UM	0.48	0.49	–
6-story	CS	0.66	0.70	0.67
	CM	0.69	0.76	0.70
	UM	0.84	0.86	–
8-story	CS	0.84	0.90	0.86
	CM	0.89	0.98	0.93
	UM	1.07	1.11	–

conducted to verify the models in nonlinear behavior terms and the results will be presented in what follows.

Eigenvalue analyses were also performed to determine the changes in the stiffness of different models after applying gravity loads. It is evident that the difference between the fundamental period of frames before and after gravity load is 8.6%, 10.8%, and 2.7% for CS, CM and UM frames respectively. This increment in CM frames is due to the lower

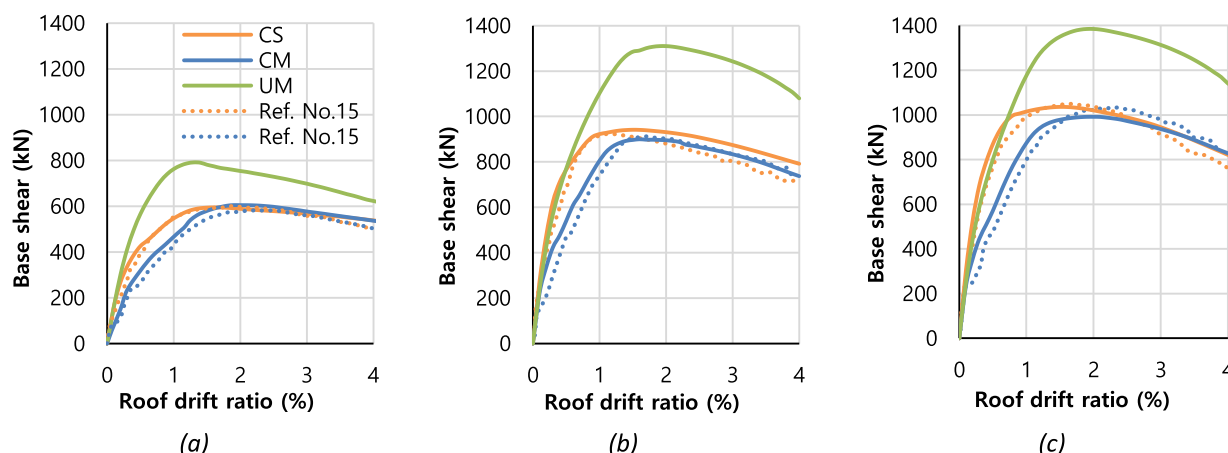


Fig. 8. Pushover curves of models: (a) 3-story, (b) 6-story, (c) 8-story.

modulus of elasticity of SMA than that of steel which leads to more deformation and cracking in concrete in CM frames compared to CS. However, in UM frames the tensile strength of UHPSFRC is higher than that of conventional concrete, which leads to undergo loads without cracking in sections compare to CS and CM models.

2.5. Pushover analysis

To assess the lateral strength and post-yield behavior of the frames, pushover analyses were performed by using a static displacement-control loading with a load pattern based on the first mode shape of the structure. The 2D pushover curves for each frame were shown in Fig. 8. It can be observed that the initial stiffness for all the frames is similar while CS has a slightly higher initial stiffness. According to this figure and by considering the differences between software and material definitions, the results coincide with a slight difference from that of the study by Alam et al. [15]. This fact verifies the modeling assumptions in terms of geometric, material, section, and element definitions in OpenSees software. Likewise, according to the pushover figures, due to improvement in material parameters in plastic hinges by using UHPSFRC, the UM frame has better performance due to its higher capacity.

3. Sequential seismic records

A total of seven mainshock-aftershock ground motion records were selected from the Pacific Earthquake Engineering Research Center

(PEER) NGA database [38] to conduct seismic sequence analysis on the frames. These real ground motion records were recorded at the same station. The magnitudes of both mainshocks and aftershocks were considered to be equal or greater than 5.0, and also the Peak Ground Acceleration (PGA) of records were selected to be greater than 0.05g [39].

Table 6 demonstrates the characteristics of the ground motions used in this study. The accumulation of energy in an earthquake is related to Arias Intensity, AI, which is presented in Eq. (4).

$$AI = \frac{\pi}{2g} \int_0^{\infty} a^2(t) dt \tag{4}$$

where g is the gravity acceleration and a(t) is the time history for the ground acceleration [40].

Fig. 9 shows the 5% damped spectral response acceleration of each selected ground motion record.

4. Technique of dynamic analysis

Each record was scaled such that the average value of the 5% damped spectral response acceleration for the selected ground motion records was not less than the design spectral acceleration for periods ranging from 0.2 T and 1.5 T, where T is the fundamental period of the frame [41]. Fig. 10 shows the 5% damped spectral response acceleration of the scaled ground motion records, and Tables 7 and 8 present the scale factors for mainshock and aftershock records, respectively.

Table 6
Mainshock-aftershock characteristics.

No.	Event name	Year	Station	Sequence	M _w	PGA (g)	AI (m/s)
R1	livermore	1980	San Ramon-Eastman Kodak	Main	5.8	0.150	0.2
				After	5.42	0.280	0.3
R2	Imperial Valley	1979	El Centro Array #3	Main	6.53	0.267	1.2
				After	5.01	0.138	0.1
R3	Irpinia, Italy	1980	Calitri	Main	6.9	0.136	0.8
				After	6.2	0.176	0.5
R4	Whittier Narrows	1987	Mt Wilson-CIT Seis Sta	Main	5.99	0.180	0.3
				After	5.27	0.155	0.1
R5	Northridge	1994	Castaic-Old Ridge Route	Main	6.69	0.568	3.2
				After	5.93	0.138	0.1
R6	Chi-Chi, Taiwan	1999	CHY035	Main	7.62	0.251	1.6
				After	6.2	0.134	0.3
R7	Northridge	1994	Moorpark-Fire Sta	Main	6.69	0.292	0.9
				After	5.93	0.184	0.2

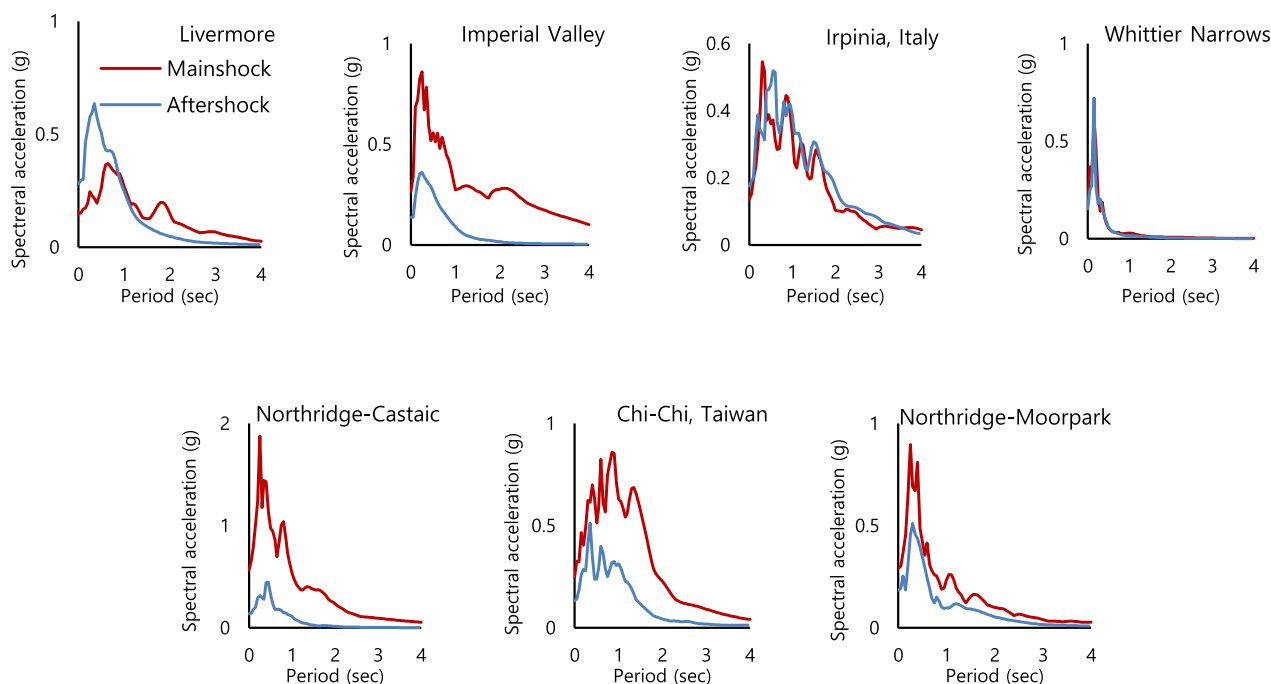


Fig. 9. The 5% damped spectral response acceleration of un-scaled records.

Nonlinear time history analyses were conducted on the initial RC-MRF model by using scaled mainshock data. Subsequently, a time gap of 40 s was considered at the end of the mainshock to allow the structure to damp the earthquake energy and vibration before the occurrence of aftershock. This gap was assumed by adding zero to the acceleration values after the mainshock and before the aftershock. The scaled aftershock record was finally applied to the damaged frame to determine the behavior of the structure under the mainshock-aftershock sequence. The time histories of the record R1 are illustrated in Fig. 11.

Moreover, to achieve the maximum damage of structures exposed to the mainshock-aftershock sequence, while the direction of the mainshock was assumed to be constant, the aftershock record was applied in both directions (negative and positive values). The maximum value of the structure response was considered as the analysis result. Fig. 12 shows the time history of roof displacement for the 6-story CS frame under R7.

5. Results and discussion

To attain the effects of seismic sequence on RC MRF drift, the transient and residual drift limits for different damage states were considered. FEMA-356 presents a range of structural performance requirements [42]. The level and damage limits determined in FEMA-356 are correlated closely with the most prevalent structural performance requirements. Table 9 presents the drift limits for both transient and residual terms according to FEMA-356 [42].

5.1. Transient inter-story drift ratio

Figs. 13 and 14 illustrate the maximum inter-story drift ratio (MIDR) due to mainshock and aftershock for 3, 6, and 8-story frames respectively.

Figs. 15 and 16 show the median MIDR for all frames in the mainshock and aftershock respectively. The transient drift limits according to FEMA-356 are shown in Figs. 13–16.

It is observed that for 3-story frames the maximum of median MIDR occurred at the first story level in mainshock and aftershock, and for 6-story frames, this occurred at the fourth story level. Regarding 8-story frames, in the case of CS and UM, the fourth story level experienced the maximum of median MIDR in mainshock and aftershock. The fifth and the sixth story levels in the 8-story CM frame showed the maximum of median MIDR in mainshock and aftershock respectively.

Considering mainshock only, in CM frames, the median MIDR is 50%, 7.5%, and 14% higher than that of CS in 3, 6, and 8-story frames, respectively, which is due to the SMA lower module of elasticity. In the UM frame, by replacing conventional concrete with UHPSFRC, the median MIDR is 17%, 24%, and 25% lower than that of CS frames in 3, 6, and 8-story frames, respectively. Although the elasticity module of UHPSFRC is lower than that of conventional concrete, its superior tensile and compressive strength result in improved performance.

In the aftershock, the median MIDR in CM frames is 40% lower than that of the CS frame for the 3-story frame, and for the 6 and 8-story frames, this is 8.9% and 5.6% higher than that of the CS frame. In the case of UM frames, the median MIDR is 35%, 31%, and 27% lower than that of CS frames in 3, 6, and 8-story frames, respectively. The results show the effect of using UHPSFRC and SMA in reducing the MIDR in aftershocks.

According to Fig. 15, 3-story CS and CM frames exceeded the IO limit, while the UM frame had a lower median MIDR than the IO limit. In 6 and 8-story frames, the CS and CM exceeded the LS limits, and the UM went beyond the IO limit state.

In the aftershock, as shown in Fig. 16, there are similar trends to the mainshock in the behavior of all frames, except for the 3-story CM frame that did not exceed the IO limit.

Fig. 17 reveals the ratio of median MIDR in aftershock to those in mainshock. It can be seen that in all frames, the upper story levels have greater potential to experience higher MIDR in the aftershock. The 8-story CS frame has the highest relative MIDR, which reaches 1.6 times in the 8th story.

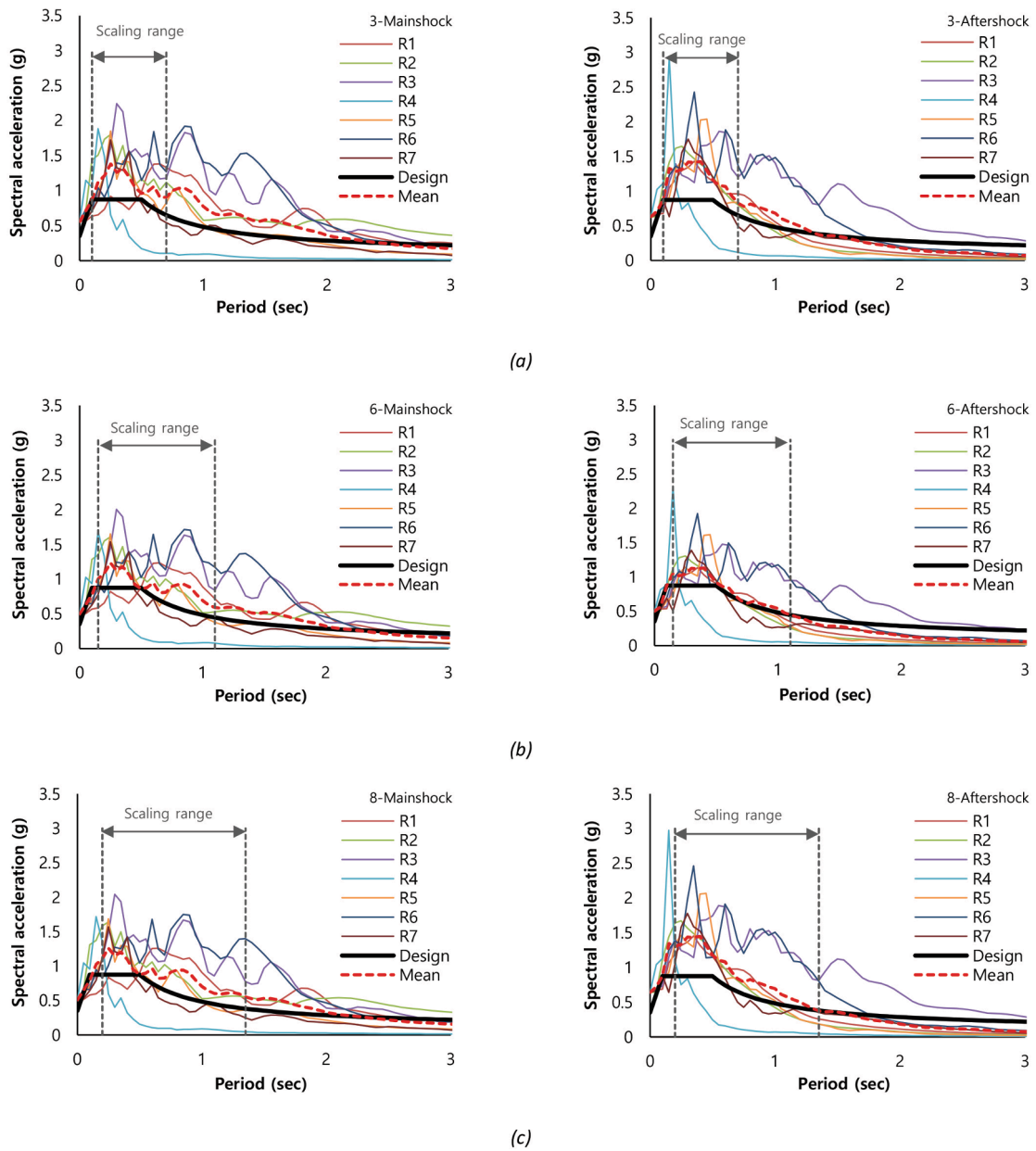


Fig. 10. The 5% damped spectral response acceleration of scaled records for: (a) 3-story frames, (b) 6-story frames, (c) 8-story frames.

Table 7
Scale factors for mainshock records.

Story ID	R1	R2	R3	R4	R5	R6	R7
3-story	3.74	2.09	4.11	3.12	0.99	2.23	1.92
6-story	3.34	1.87	3.67	2.78	0.88	1.99	1.71
8-story	3.41	1.91	3.74	2.84	0.90	2.03	1.75

Table 8
Scale factors for aftershock records.

Story ID	R1	R2	R3	R4	R5	R6	R7
3-story	2.25	4.56	3.58	4.06	4.55	4.72	3.42
6-story	1.79	3.62	2.84	3.22	3.61	3.74	2.71
8-story	2.29	4.64	3.64	4.12	4.62	4.79	3.47

5.2. Transient roof drift ratio

Figs. 18–20 indicate the maximum roof drift ratio (MRDR) in mainshock and aftershock for 3, 6, and 8-story frames respectively. It is observed that for 3-story frames, in mainshock the median MRDR for the CM frame is 57% higher and for the UM frame, it is 18% lower than the CS frame. However, in the aftershock, the medians MRDR for the CM and UM frame are 16% and 19% lower than that of the CS frame respectively.

In 6-story frames in mainshock, the CM frame has 17% higher median MRDR in comparison with the CS frame and UM has a similar median MRDR to the CS frame. In aftershock, it is 45% and 42% lower for the CM frame and UM frames, respectively.

In 8-story frames, in the mainshock, the median MRDR for the CM frame is 49% higher and for the UM frame, it is 8% lower than the CS frame, while in the aftershock, it is 14% higher for the CM frame and the UM frame, it is 25% lower than the CS frame.

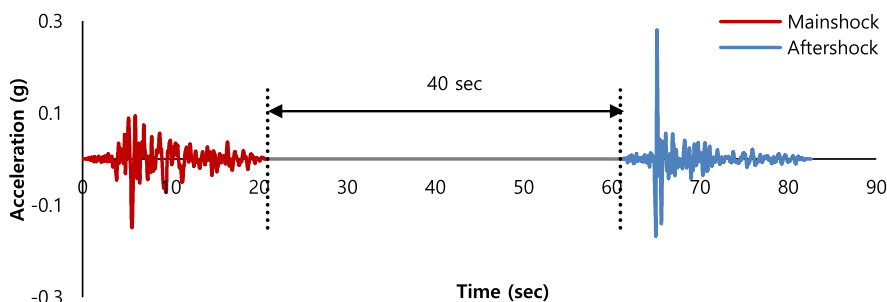


Fig. 11. Acceleration time history for mainshock-aftershock sequence of R1.

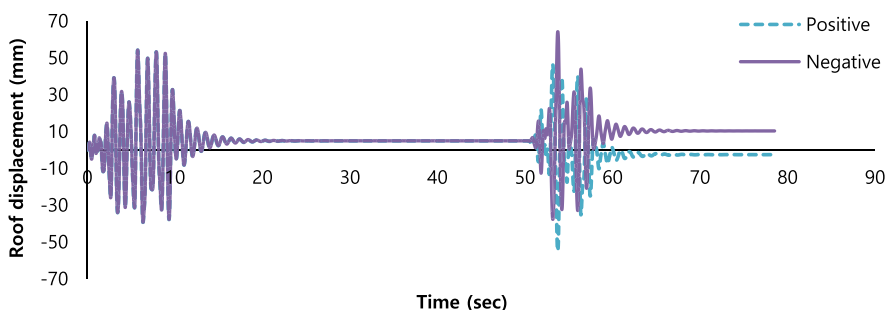


Fig. 12. The effect of aftershock direction on the 6-story CS frame.

Table 9
Drift limits according to FEMA-356 [42].

Performance level	Drift limit		Damage definition	
	Transient	Residual	Primary	Secondary
IO	1%	Negligible	Minor hairline cracking, Limited yielding at a few parts, No crushing.	Minor spalling in a few locations in ductile elements, Flexural cracking in elements.
LS	2%	1%	Extensive damage to beams, Spalling of cover and shear cracking for ductile columns, Minor spalling in non-ductile columns.	large cracks and occurrence of hinges in ductile elements, Limited cracks or failure in some non-ductile columns, Serious damage in short columns.
CP	4%	2%	large cracks and occurrence of hinges in ductile elements, Limited cracks or failure in some non-ductile columns, Serious damage in short columns.	Widespread spalling in elements, Serious joint damage, Some rebars buckled.

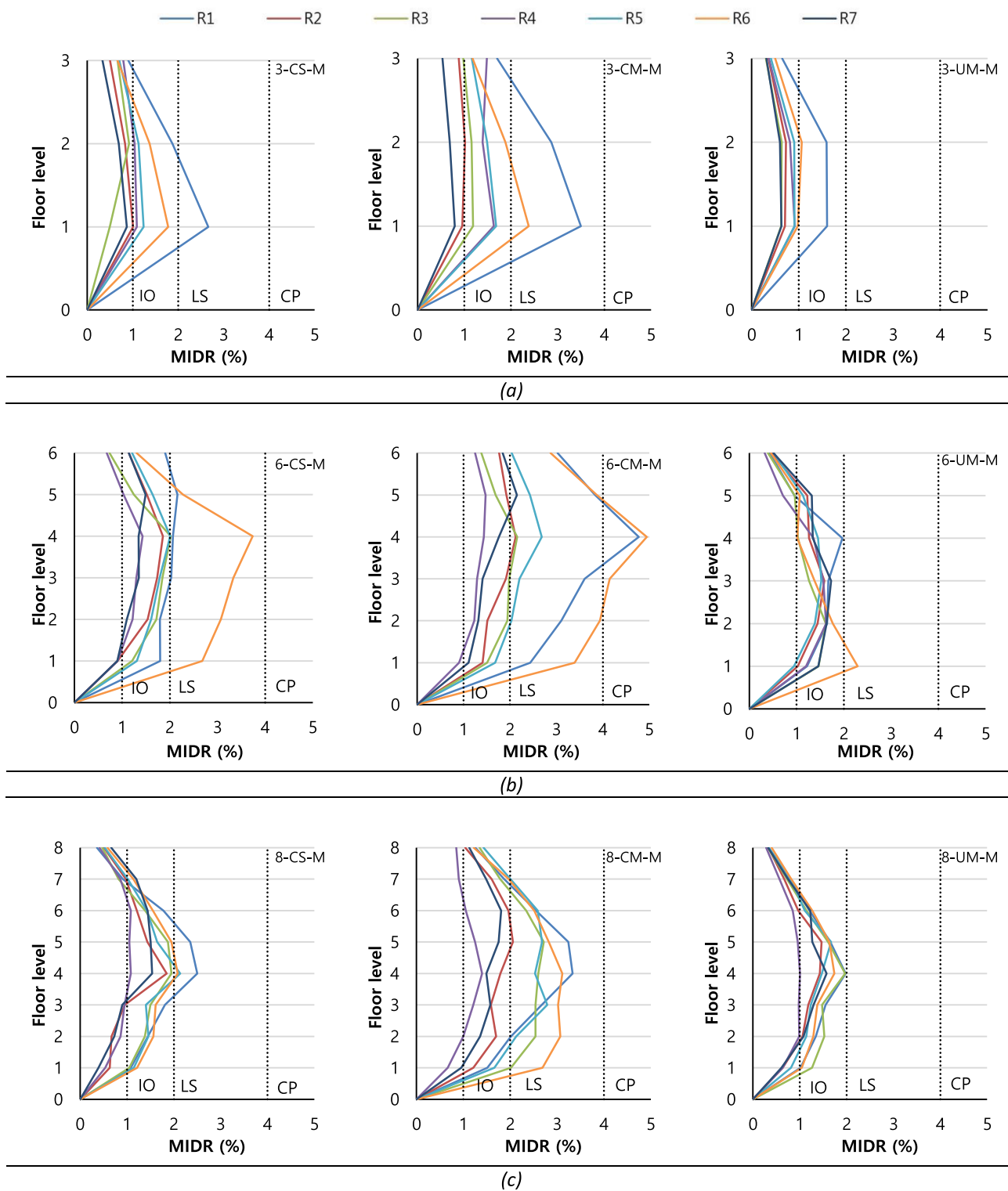


Fig. 13. MIDR in mainshock: (a) 3-story frames, (b) 6-story frames, (c) 8-story frames.

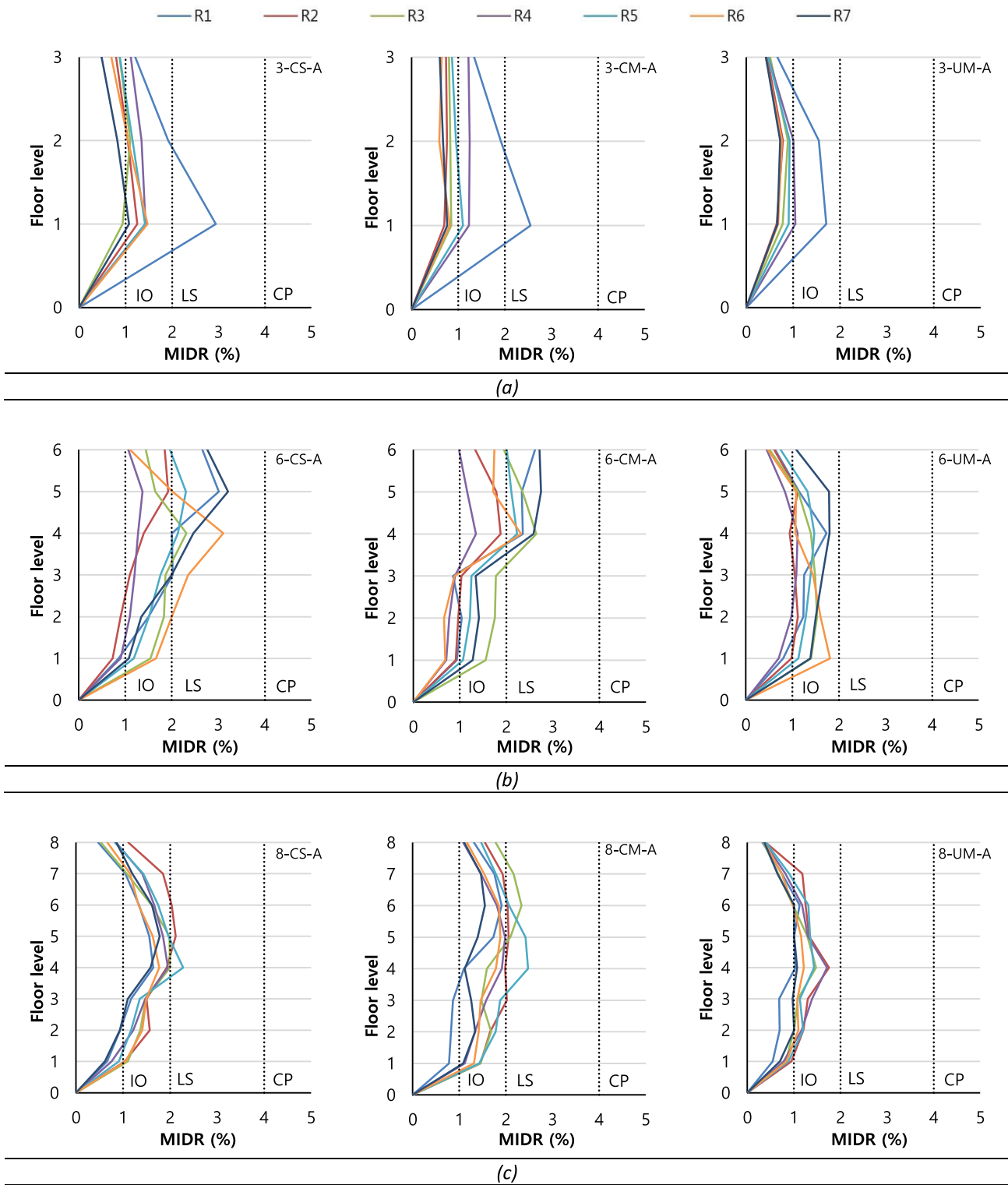


Fig. 14. MIDR in aftershock: (a) 3-story frames, (b) 6-story frames, (c) 8-story frames.

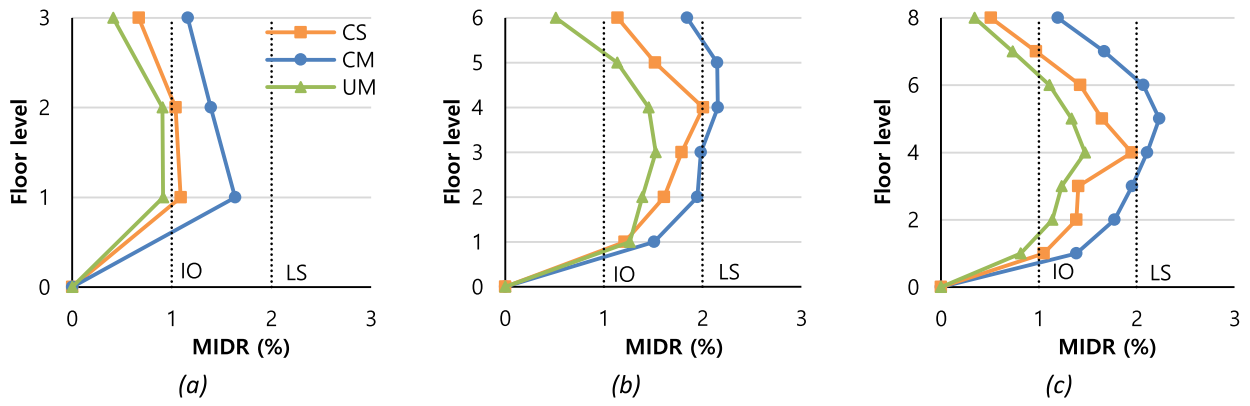


Fig. 15. The median MIDR in mainshock: (a) 3-story frames, (b) 6-story frames, (c) 8-story frames.

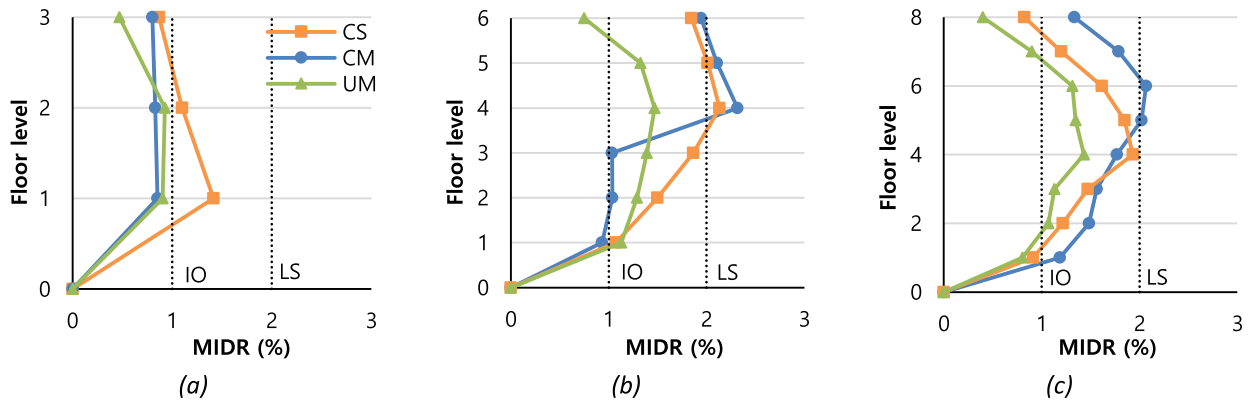


Fig. 16. The median MIDR in aftershock: (a) 3-story frames, (b) 6-story frames, (c) 8-story frames.

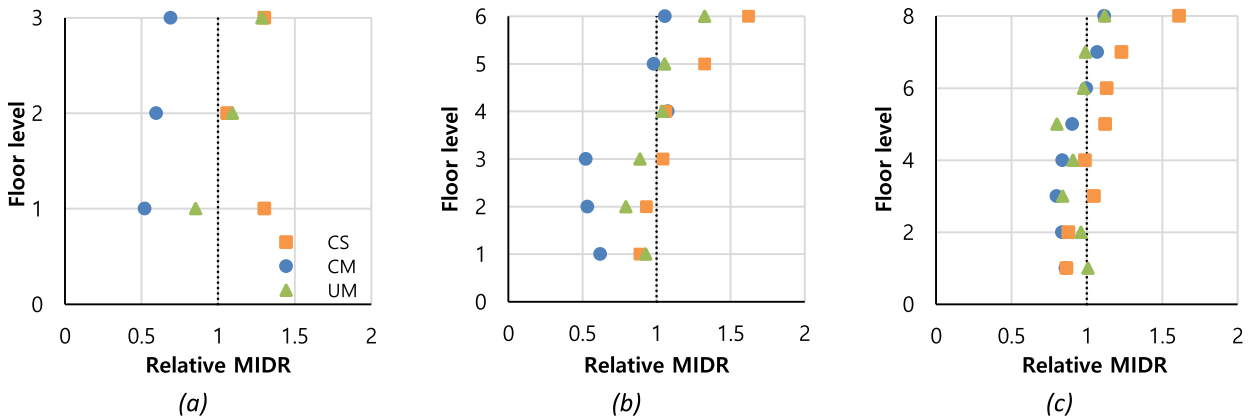


Fig. 17. Relative MIDR (aftershock/mainshock): (a) 3-story frames, (b) 6-story frames, (c) 8-story frames.

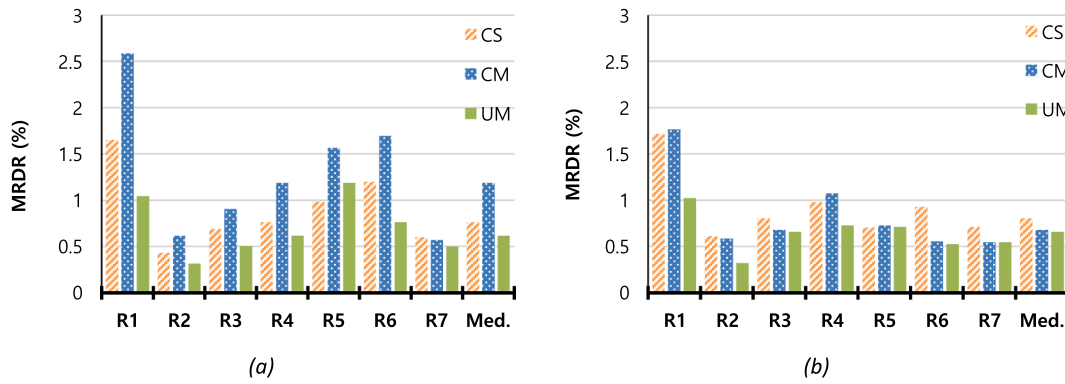


Fig. 18. The MRDR for 3-story frames: (a) Mainshock, (b) Aftershock.

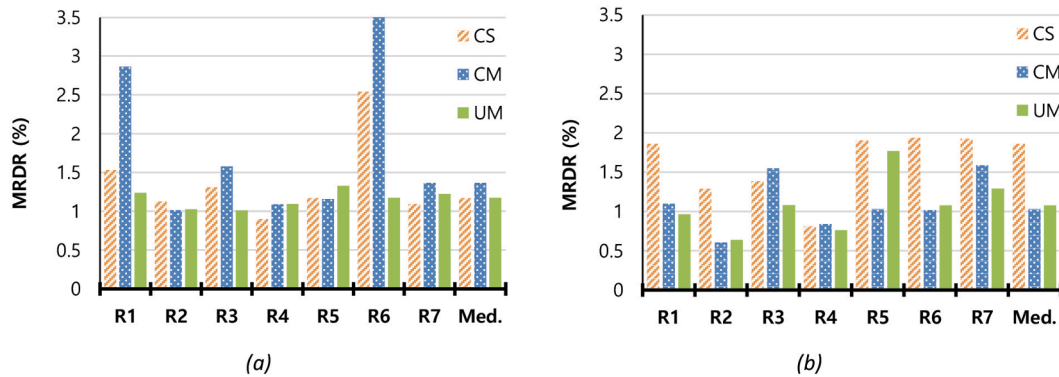


Fig. 19. The MRDR for 6-story frames: (a) Mainshock, (b) Aftershock.

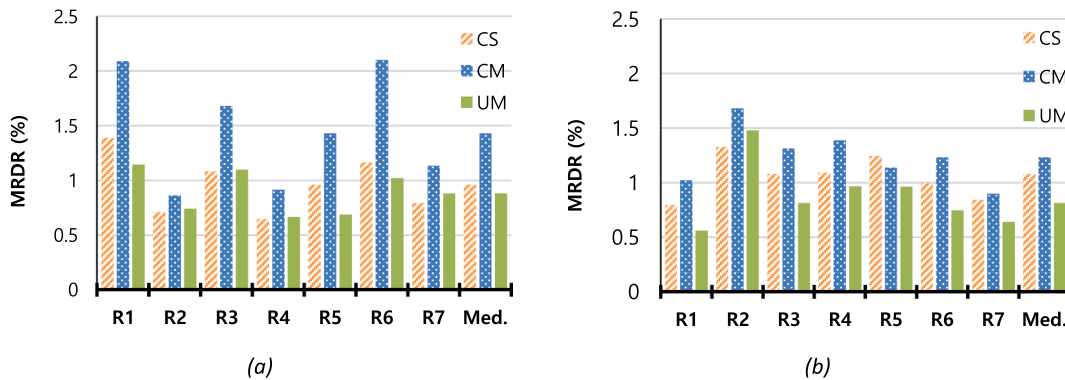


Fig. 20. The MRDR for 8-story frames: (a) Mainshock, (b) Aftershock.

Overall, in both mainshock and aftershock, UM frames have the lowest median MRDR in 3, 6, and 8-story frames. In the mainshock, CM frames have the highest median MRDR in 3, 6, and 8-story frames. But in the aftershock, CS frames have the highest median MRDR in the 3 and 6-story frames. In the case of 8-story frames in the aftershock, the CM frame experienced higher median MRDR compared to the CS frame, while the ratio decreases compared to the mainshock (49% in mainshock and 14% in aftershock).

This trend could be associated with the shape recovery of SMA and the high strength of UHPSFRC in compression and tension.

5.3. Residual inter-story drift ratio

It is essential to consider the residual drifts to evaluate the performance of a structure not only after an earthquake and during the following seismic sequences, but also to make any decisions about

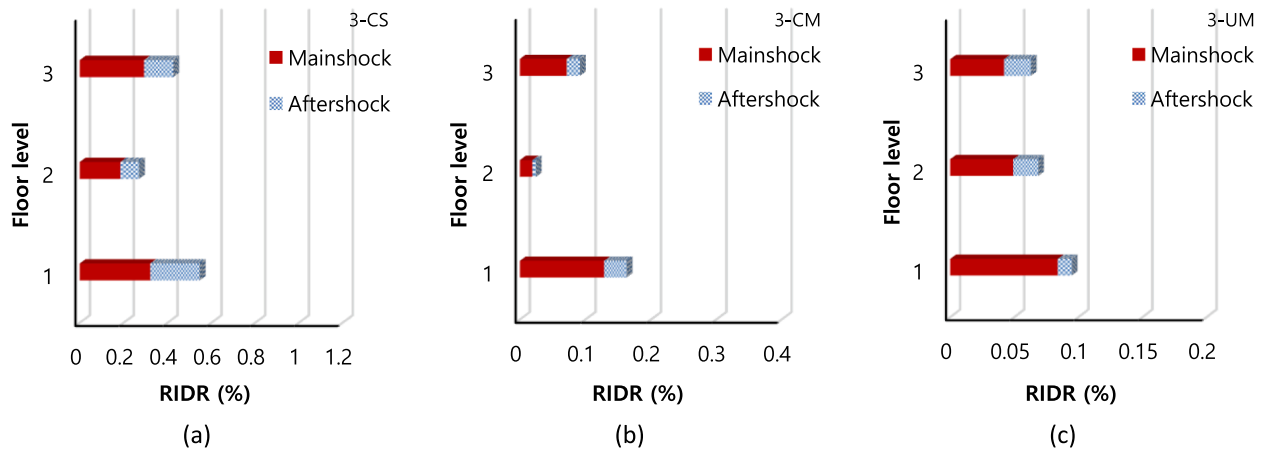


Fig. 21. The median RIDR for 3-story frames: (a) CS, (b) CM, (c) UM.

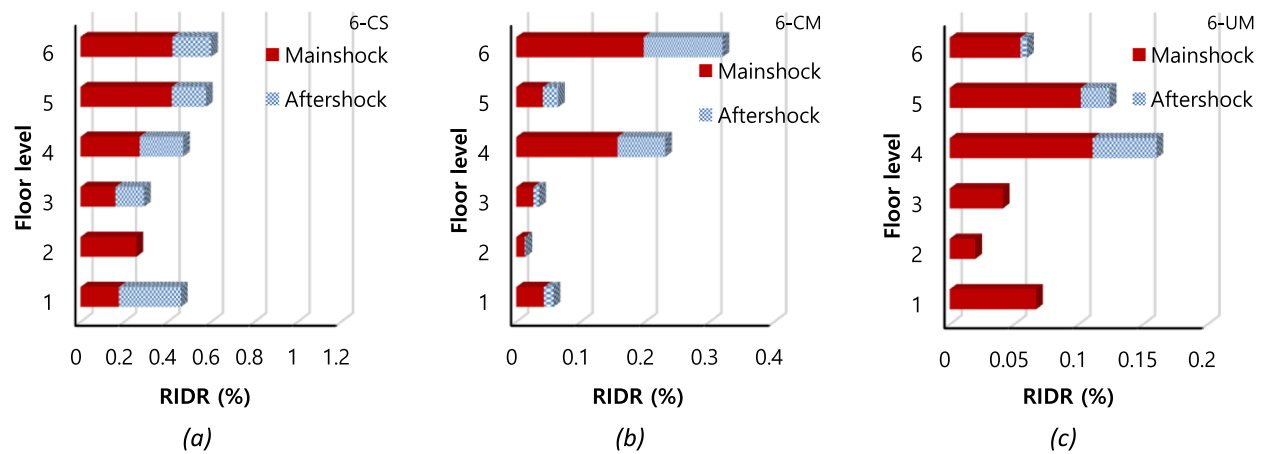


Fig. 22. The median RIDR for 6-story frames: (a) CS, (b) CM, (c) UM.

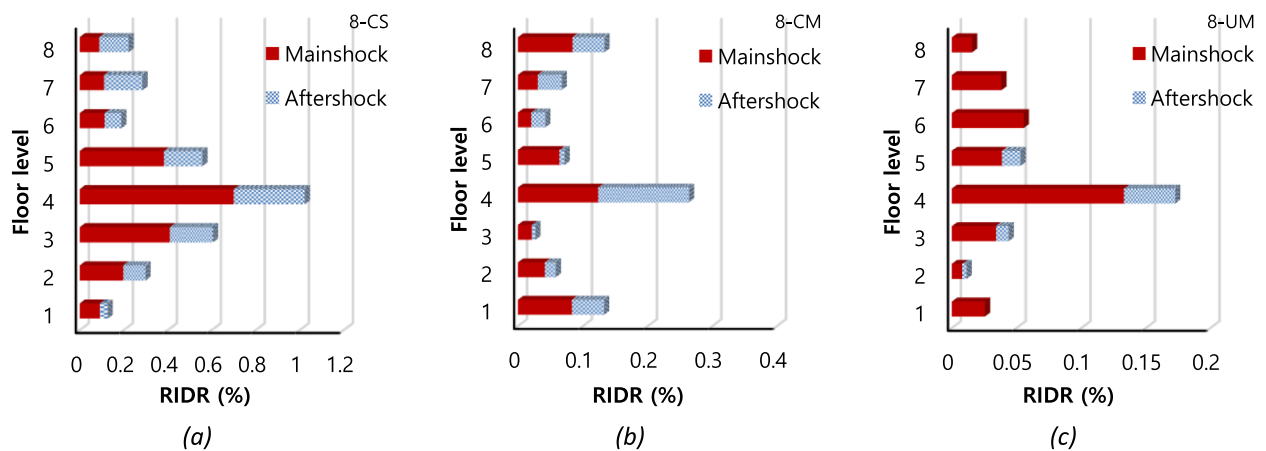


Fig. 23. The median RIDR for 8-story frames: (a) CS, (b) CM, (c) UM.

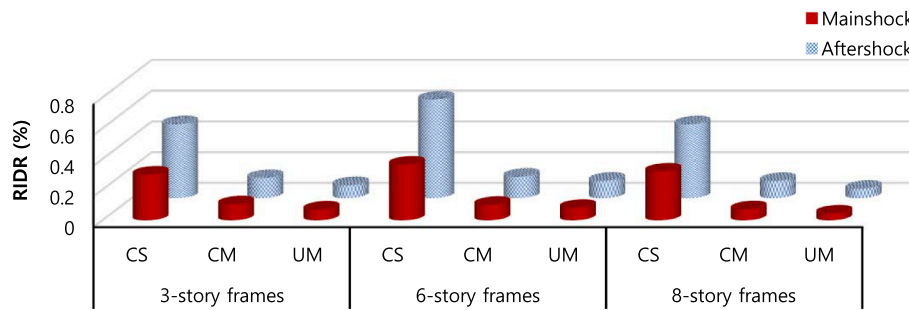


Fig. 24. Mean RIDR for 3, 6, and 8-story frames.

retrofitting or repairing. Residual drifts were calculated by continuing the analysis for some seconds by adding zero values to the end of the main and aftershock records.

Results from dynamic time history analysis indicated that residual inter-story drift ratio (RIDR) of CM and UM frames in all story levels in all records in both mainshock and aftershock did not reach the LS limit (1%), while for CS frames some story levels reach the LS and CP limit in some records.

The median RIDR for the frames are exhibited in Figs. 21–23. It is observed that for all 3-story frames the median RIDR occurred at the first story level in mainshock, while for 6-story CS and CM frames, this occurred at the sixth story level. For the 6-story UM frame and all 8-story frames, this occurred at the fourth story level. In aftershock, the median RIDR for all frames occurred in that story level with the highest median RIDR in the mainshock.

As expected, all CS and UM frames experienced the highest and lowest median RIDR demand respectively in both mainshock and aftershock.

According to Fig. 21 for the 3-story frames, the following results can be obtained:

- In mainshock: CM and UM frames experienced 59% and 75% lower RIDR demand compared to that of the CS frame, respectively.
- In aftershock: CM and UM frames experienced 71% and 84% lower RIDR demand compared to that of the CS frame, respectively.

From Fig. 22 for the 6-story frames:

- The RIDR demand for CM and UM frames was 57% and 77% lower than that of the CS frame, respectively in the mainshock.
- The RIDR demand for CM and UM frames was 47% and 73% lower than that of the CS frame, respectively in the aftershock.

For 8-story frames (Fig. 23):

- CM and UM frames in the mainshock have 83% and 81% lower RIDR demand in comparison with that of the CS frame, respectively.
- CM and UM frames in the aftershock have 75% and 83% lower RIDR demand in comparison to that of the CS frame, respectively.

Overall, the synergistic effect of using SMA and UHPSFRC leads to a considerable decrease in median RIDR.

Fig. 24 represents the mean RIDR for all frames to elucidate the general behavior of frames in terms of residual drifts. It is evident that all frames experience higher mean RIDR in the aftershock compared to the

mainshock. This increase for CS frames is 61%, 77%, and 51% in 3, 6, and 8-story frames, respectively. In the case of CM frames, this increase is 26%, 39%, and 56% for 3, 6, and 8 story frames, respectively. 3, 6, and 8-story UM frames experienced 21%, 40%, and 36% more mean RIDR in the aftershock, respectively.

Additionally, in all story levels, CS frames have the highest mean RIDR, while UM frames have the lowest value of mean RIDR in both mainshock and aftershock. In 3-story frames, the CS, CM and UM frame have the mean RIDR value of 0.36%, 0.10% and 0.07% in the mainshock and 0.48%, 0.13% and 0.09% in the aftershock, respectively. The mean RIDR in 6-story frames, for CS, CM and UM in the mainshock is 0.36%, 0.10% and 0.08% and in the aftershock, it is 0.64%, 0.14% and 0.11%, respectively. In 8-story frames, the CS, CM and UM frame experienced a mean RIDR value of 0.32%, 0.07% and 0.05% in the mainshock and 0.48%, 0.11% and 0.06% in the aftershock, respectively.

Furthermore, from Fig. 24 it could be observed that the 6-story CS frame is the most vulnerable frame to damage in both the mainshock and aftershock.

6. Conclusions

This study was conducted to assess the improved behavior of RC frames incorporating SMA and UHPSFRC as novel materials in the plastic hinge length of the beams and to provide a comparison between transient and residual drifts. Three different heights of each frame type were considered. Dynamic time history analysis was conducted by considering seven real mainshock-aftershock records to evaluate the effects of pre-existing damage in different cases. The following are the main conclusion of this study:

- In both mainshock and aftershocks, CM frames had the highest median MIDR in almost all cases, and UM frames experienced the lowest median MIDR and did not exceed the LS limit.
- In both mainshock and aftershock, UM frames have the lowest median MRDR. CM frames have the highest median MRDR in mainshock, but in aftershock about all CS frames have the highest median MRDR.
- The RIDR for CM and UM frames in all story levels for all records in both mainshock and aftershock did not reach the LS limit. All CS and UM frames experienced the highest and lowest median RIDR demand respectively in both mainshock and aftershock.
- All frames experience higher mean RIDR in aftershock than in mainshock. Additionally, in all story levels, CS frames have the highest mean RIDR while UM frames have the lowest value of mean RIDR in both mainshock and aftershock.

In conclusion, using SMA in the plastic hinge of beams (i.e., CM frames) causes a decrease in residual drifts, but it leads to an increase in transient drifts, which is obvious in the mainshock. However, the synergistic effect of using SMA and UHPFRC (i.e., UM frames) leads to a considerable decrease in residual and transient drifts in both mainshock and aftershock. By reducing residual drifts, the post-earthquake functionality of the structure will increase and the cost of repair will decrease. This fact shows the necessity of designing low damage and high-performance structures.

It is of great significance that this paper was a primary study and has the following limitations that could be considered for future researches: using a large set of real and artificial seismic sequences is proposed to more thoroughly estimate structural performance under seismic loads. Moreover, because UHPFRC has higher strength compared to conventional concrete and SMA has a lower modulus of elasticity compared to steel, further study is needed to develop a performance-based design procedure for these types of frames. The accuracy of numerical modeling could be improved by considering slippage between different types of rebar and concrete materials. Experimental research is also needed to study the seismic behavior of frames with SMA and UHPFRC under shake table loading.

Declaration of Competing Interest

The authors declare that they have no known competing financial interests or personal relationships that could have appeared to influence the work reported in this paper.

Acknowledgement

The authors received no financial support for the research, authorship, and publication of this article.

References

- [1] U.S. Geological Survey (2019), <https://www.usgs.gov/>.
- [2] Hauksson E, Jones LM, Hutton K. The 1994 Northridge earthquake sequence in California: Seismological and tectonic aspects. *Geol Res* 1995;100(B7):12335–55. <https://doi.org/10.1029/95JB00865>.
- [3] USGS (2000), "Implications for earthquake risk reduction in the United States from the Kocaeli, Turkey, Earthquake of August 17, 1999", Circular No. 1193; U.S. Geological Survey, Reston, VA.
- [4] Moss RES, Thompson EM, Kieffer DS, et al. Geotechnical effects of the 2015 magnitude 7.8 Gorkha, Nepal, earthquake and aftershocks. *Seismol Res Lett* 2015; 86(6):1514–23. <https://doi.org/10.1785/0220150158>.
- [5] Guo X, He Zh, Xu J. Identification of incremental seismic damage development in RC structures excited with sequence-type ground motions. *Structures* 2020;24: 464–76. <https://doi.org/10.1016/j.istruc.2020.01.012>.
- [6] Raghunandan M, Liel AB, Luco N. Aftershock collapse vulnerability assessment of reinforced concrete frame structures. *Earthquake Eng Struct Dyn* 2015;44(3): 419–39. <https://doi.org/10.1002/eqe.v44.3.10.1002/eqe.2478>.
- [7] Jeon J-S, DesRoches R, Lowes LN, Brilakis I. Framework of aftershock fragility assessment-case studies: older California reinforced concrete building frames. *Earthquake Eng Struct Dyn* 2015;44(15):2617–36. <https://doi.org/10.1002/eqe.v44.15.10.1002/eqe.2599>.
- [8] Furtado A, Rodrigues H, Varum H, Arede A. Mainshock-aftershock damage assessment of infilled RC structures. *Eng Struct* 2018;175:645–60. <https://doi.org/10.1016/j.engstruct.2018.08.063>.
- [9] Shafaei H, Naderpour H. Seismic fragility evaluation of FRP-retrofitted RC frames subjected to mainshock-aftershock records. *Structures* 2020;27:950–61. <https://doi.org/10.1016/j.istruc.2020.07.018>.
- [10] Dong Y, Frangopol DM. Risk and resilience assessment of bridge under mainshock and aftershocks incorporating uncertainties. *Eng Struct* 2015;83:198–208. <https://doi.org/10.1016/j.engstruct.2014.10.050>.
- [11] TahamouliRoudsari M, Entezari A, Hadidi MH, Gandomian O. Experimental assessment of retrofitted RC frames with different steel braces. *Structures* 2017;11: 206–17. <https://doi.org/10.1016/j.istruc.2017.06.003>.
- [12] Vakili SE, Homami P, Esfahani MR. Effect of fibers and hybrid fibers on the shear strength of lightweight concrete beams reinforced with GFRP bars. *Structures* 2019;20:290–7. <https://doi.org/10.1016/j.istruc.2019.04.006>.
- [13] Mirtahteri M, Amini M, Khorshidi H. Incremental dynamic analyses of concrete buildings reinforced with shape memory alloy. *Steel Compos Struct* 2017;23(1): 95–105. <https://doi.org/10.12989/scs.2017.23.1.095>.
- [14] Nehdi M, Alam MS, Youssef MA. Development of corrosion-free concrete beam-column joint with adequate seismic energy dissipation. *Eng Struct* 2009;32(9): 2518–28. <https://doi.org/10.1016/j.engstruct.2010.04.020>.
- [15] Alam MS, Moni M, Tesfamariam S. Seismic overstrength and ductility of concrete buildings reinforced with superelastic shape memory alloy bar. *Eng Struct* 2012; 34:8–20. <https://doi.org/10.1016/j.engstruct.2011.08.030>.
- [16] Billah AHMM, Alam MS. Bond behavior of smooth and sand-coated shape memory alloy (SMA) rebar in concrete. *Structures* 2016;5:186–95. <https://doi.org/10.1016/j.istruc.2015.11.005>.
- [17] Zafar A, Andrewes B. Seismic behavior of SMA-FRP reinforced concrete frames under sequential seismic hazard. *Eng Struct* 2015;98:163–73. <https://doi.org/10.1016/j.engstruct.2015.03.045>.
- [18] Gomez AN, Bonet JL. Improving the seismic behavior of reinforced concrete moment resisting frame by means of SMA bars and ultra-high-performance concrete. *Eng Struct* 2019;197:109409. <https://doi.org/10.1016/j.engstruct.2019.109409>.
- [19] Pereiro-Barceló J, Bonet JL, Gómez-Portillo S, Castro-Bugallo C. Ductility of high-performance concrete and very-high-performance concrete elements with Ni-Ti reinforcements. *Constr Build Mater* 2018;175:531–51. <https://doi.org/10.1016/j.conbuildmat.2018.04.172>.
- [20] Dehghani A, Mozafari AR, Aslani F. Evaluation of the efficacy of using engineered cementitious composites in RC beam-column joints. *Structures* 2020;27:151–62. <https://doi.org/10.1016/j.istruc.2020.05.045>.
- [21] Zhang R, Matsumoto K, Hirata T, Ishizeki Y, Niwa J. Application of PP-ECC in beam-column joint connections of rigid-framed railway bridges to reduce transverse reinforcements. *Eng Struct* 2015;86:146–56. <https://doi.org/10.1016/j.engstruct.2015.01.005>.
- [22] Fanaie N, Nazari M, M., Cyclic behavior of extended end-plate connections with shape memory alloy bolts. *Struct Eng Mech* 2016;60(3):507–27. <https://doi.org/10.12989/sem.2016.60.3.507>.
- [23] Shahverdi M, Michels J, Czaderski Ch, Motavalli M. Iron-base shape memory alloy strips for strengthening RC members: Material behavior and characterization. *Constr Build Mater* 2018;173:586–99. <https://doi.org/10.1016/j.conbuildmat.2018.04.057>.
- [24] Alam MS, Youssef MA, Nehdi M. Utilizing shape memory alloys to enhance the performance and safety of civil infrastructure: a review. *Can J Civ Eng* 2007;34(9): 1075–86. <https://doi.org/10.1139/107-038>.
- [25] Said SH, Razak HA, Othman I. Strength and deformation characteristics of engineered cementitious composite slabs with different polymer fibers. *Reinforced Plast Compos* 2015;34(23):1950–62. <https://doi.org/10.1177/0731684415607393>.
- [26] He LX, Wu Ch, Li J. Post-earthquake evaluation of damage and residual performance of UHPFRC piers based on nonlinear model updating. *Sound Vib* 2019;448:53–72. <https://doi.org/10.1016/j.jsv.2019.02.011>.
- [27] Pauly T, Priestley MNJ. *Seismic Design of Reinforced Concrete and Masonry Buildings*. New York, NY, USA: A Wiley Interscience Publication; 1992.
- [28] Alam MS, Youssef MA, Nehdi M. Analytical prediction of the seismic behavior of superelastic shape memory alloy reinforced concrete elements. *Eng Struct* 2008;30 (12):3399–411. <https://doi.org/10.1016/j.engstruct.2008.05.025>.
- [29] Mazzoni S, McKenna F, Scott MH, Fenves GL. *OpenSees Command Language Manual*. Pacific Earthquake Engineering Research Centre: University of California, Berkeley, CA, USA; 2007.
- [30] Mander JB, Priestley MJN, Park R. Theoretical stress-strain model for confined concrete. *Struct Eng* 1998;114(8):1804–26.
- [31] Menegotto, M. and Pinto, P.E. (1973), "Method of analysis of cyclically loaded RC plane frames including changes in geometry and non-elastic behavior of elements under normal force and bending", Research Report No.13; Proceedings of IABSE Symposium on Resistance and Ultimate Deformability of Structures.
- [32] Han TS, Feenstra PH, Billington SL. Simulation of highly ductile fiber-reinforced cement-based composite components under cyclic loading. *ACI Struct J* 2003;100 (6):749–57.
- [33] Xu Sh, Wu Ch, Liu Zh, Han K, Su Y, Zhao J, et al. Experimental investigation of seismic behavior of ultra-high-performance steel fiber reinforced concrete columns. *Eng Struct* 2017;152:129–48. <https://doi.org/10.1016/j.engstruct.2017.09.007>.
- [34] D. Fugazza "Shape-memory alloy devices in earthquake engineering: mechanical properties, constitutive modelling and numerical simulations", Master's Thesis, European School for Advanced Studies in Reduction of Seismic Risk (ROSE School) 2003 Pavia.
- [35] Auricchio F, Sacco E. A one-dimensional model for superelastic shape-memory alloys with different elastic properties between austenite and martensite. *Int J Non Linear Mech* 1997;32(6):1101–14. [https://doi.org/10.1016/S0020-7462\(96\)00130-8](https://doi.org/10.1016/S0020-7462(96)00130-8).

- [36] Youssef MA, Alam MS, Nehdi M. Experimental investigation on the seismic behavior of beam-column joints reinforced with superelastic shape memory alloys. *J Earthquake Eng* 2008;12:1205–22. <https://doi.org/10.1080/13632460802003082>.
- [37] Zhao J, Sritharan S. Modeling of strain penetration effects in fiber-based analysis of reinforced concrete structures. *ACI Struct J* 2007;104(2):133–41.
- [38] PEER, NGA database (2019), <http://ngawest2.berkeley.edu/>.
- [39] Silwal B, Ozbulut E, O.,. Aftershock fragility assessment of steel moment frames with self-centering dampers. *Eng Struct* 2018;168:12–22. <https://doi.org/10.1016/j.engstruct.2018.04.071>.
- [40] Arias A. a Measure of Earthquake Intensity. In: Hansen RJ, editor. *Seismic design for nuclear power plants*, MIT Press. USA: Massachusetts; 1970.
- [41] ASCE, SEL. 7–16. *Minimum Design Loads for Buildings and Other Structures*. Virginia: American Society of Civil Engineers; 2016.
- [42] FEMA. *Prestandard and Commentary for the Seismic Rehabilitation of Buildings*, FEMA-356. Washington DC, USA: Federal Emergency Management Agency; 2000.